analytical chemistry

Article

Cite This: Anal. Chem. 2018, 90, 2238−2245

pubs.acs.org/ac

A Numerical Study on the Effect of Particle Surface Coverage on the Quartz Crystal Microbalance Response

Jurriaan J. J. Gillissen,[†,‡] Joshua A. Jackman,[†,‡] Seyed R. Tabaei,[†,‡] and Nam-Joon Cho*[,†,‡,§]

[†]School of Materials Science and Engineering, Nanyang Technological University, 50 Nanyang Avenue 639798, Singapore

[‡]Centre for Biomimetic Sensor Science, Nanyang Technological University, 50 Nanyang Drive 637553, Singapore

[§]School of Chemical and Biomedical Engineering, Nanyang Technological University, 62 Nanyang Drive 637459, Singapore

Supporting Information

ABSTRACT: The quartz crystal microbalance (QCM) is a surface-sensitive measurement technique to characterize adsorption processes at solid−fluid interfaces. While QCM measurements are routinely applied to study homogeneous thin films, characterizing heterogeneous films of adsorbed particles remains challenging because QCM is sensitive to not only the mass of adsorbed particles but also to that of hydrodynamically coupled fluid. To extract information about adsorbed particles, it is necessary to model these hydrodynamic effects, however, current QCM models are restricted to the limit of either a very low surface coverage or to the extrapolated limit of saturation coverage. Herein, we investigated QCM measurement responses in the intermediate surface coverage regime, by conducting lattice Boltzmann simulations of monodisperse, spherical particles that are attached to an oscillating surface. From the simulations, we relate the overtone-dependent QCM frequency and bandwidth shifts to particle size, interparticle distance, and the relevant hydrodynamic length scale. The corresponding results are in qualitative agreement with experimental QCM data for sub-100 nm, gel-phase liposomes. Furthermore, the data provide a theoretical basis for extracting particle sizes from QCM data in the high surface coverage limit.

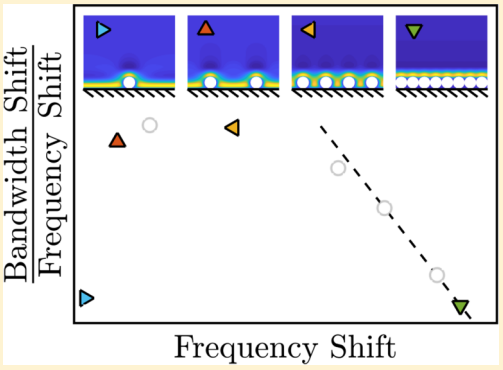

The quartz crystal microbalance (QCM) is a widely used, surface-sensitive measurement technique to characterize adsorption events at solid−fluid interfaces.[1,2] QCM measurements involve tracking the resonance behavior of shear-thickness oscillations of a piezoelectric quartz crystal at its fundamental frequency and odd overtones thereof.[3,4] The presence of an adsorbate on the QCM sensor surface influences this resonance behavior, and corresponding shifts can be monitored in order to obtain information about physical properties of the adsorbate.[5,6]

The QCM detects not only the adlayer but also the fluid that is coupled to the oscillating adlayer.[7,8] As a result, translating QCM data to adlayer properties requires so-called "QCM models", which are based on hydrodynamic analysis. Analytical QCM models have been developed to extract the mass and viscoelastic properties of homogeneous, thin-film adsorbates.[9−12] On the other hand, layers of adsorbed particles are governed by heterogeneous hydrodynamic coupling between the adlayer and surrounding fluid.[3,12−20] These complex hydrodynamic effects have hindered the development of corresponding QCM models that relate QCM measurement responses, via the hydrodynamic force, to the properties of adsorbed particles, for example, surface coverage, size, and shape. As a result, current QCM models are restricted to the limit of either a very low surface coverage[21,22] or to the extrapolated limit of saturation coverage.[23,24] Specifically, this latter model extrapolates QCM data to a hypothetical scenario, where the adsorbed particles behave as a rigid, densely packed layer. The thickness of the corresponding adlayer is determined by using a simple analytical model, which is valid for homogeneous films.[9] In some cases, the resulting adlayer thickness agreed well with the known size of adsorbed particles.[23−27] However, a theoretical basis for this "extrapolation method" remains to be established.

Constructing such theory requires analyzing the hydrodynamic force acting on a collection of particles attached to an oscillating surface. Previously, we combined numerical simulation with dimensional analysis to study the corresponding problem for a single spherical[21] or ellipsoidal[22] particle. From those analyses, we derived QCM models for extracting the size and shape of adsorbed particles at low QCM surface coverages.[21,22] Herein, we extend this methodology and investigate the hydrodynamics of adsorbed particles, not only for a low surface coverage but also for higher surface coverages where hydrodynamic interactions between adsorbed particles are important. By systematically varying the independent, dimensionless parameters in the simulation, we provide a comprehensive description of the hydrodynamic interaction

Received: November 7, 2017
Accepted: December 14, 2017
Published: December 14, 2017

DOI: 10.1021/acs.analchem.7b04607
Anal. Chem. 2018, 90, 2238−2245

between monodisperse, spherical particles adsorbed on the QCM sensor surface, as a function of particle size and surface coverage. Guided by the simulation outcome, we also provide a theoretical basis for the aforementioned extrapolation method to determine the size of adsorbed particles from QCM data at high surface coverages.

THEORETICAL CONSIDERATIONS

We consider the QCM measurement response that occurs due to the adsorption of N solid, spherical particles of radius a. The surface area of the quartz crystal is A_Q and the distance between the adsorbed particles is $L = (A_Q/N)^{1/2}$, which corresponds to a surface coverage of $\phi = \pi(a/L)^2$. We assume that the particles are rigidly adhered to the substrate and remain spherical in the adsorbed state. $\Delta\hat{F}$ denotes the complex-valued amplitude of the force oscillation, which is exerted on the quartz crystal due to the adsorption of one particle, and the hat $\hat{}$ signifies a complex number. The force amplitude, $\Delta\hat{F}$, has an inertial (real $\mathcal{R}$) component, which is in phase with the quartz acceleration and responsible for the frequency shift, Δf, and a dissipative (imaginary $\mathcal{J}$) component, which is in phase with the quartz velocity and responsible for the bandwidth shift, $\Delta\Gamma = f\Delta D/\pi$. The bandwidth shift is equivalent to the dissipation shift, ΔD, where $f = f_0 n = \omega/2\pi$ is the (overtone) frequency, n is the overtone number, f_0 is the fundamental frequency, and ω is the (overtone) angular frequency of the quartz. In this work, the QCM data is presented in terms of the frequency and bandwidth shifts (Δf, $\Delta\Gamma$). Since $\Delta\Gamma$ is dimensionally equivalent to Δf, this representation offers a seamless comparison between the two quantities. It also allows us to compare our theoretical approach with the extrapolation method, which was described in the first section of this Article, and is henceforth referred to as the $\Delta\Gamma/\Delta f$ extrapolation method. Specifically, the $\Delta\Gamma/\Delta f$ extrapolation method involves plotting the $-\Delta\Gamma/\Delta f$ ratio versus $-\Delta f/n$ at multiple overtones, n, in order to determine the adlayer height.[23,24]

Based on the above definitions, the QCM frequency shift, Δf, and bandwidth shift, $\Delta\Gamma$, can be expressed as follows:[3,4]

$$-\Delta f + i\Delta\Gamma = \frac{fN\Delta\hat{F}}{\omega U m_Q} \tag{1}$$

where $m_Q = A_Q l_Q \rho_Q$ is the mass, l_Q is the thickness and ρ_Q is the mass density of the quartz crystal, and $i = \sqrt{-1}$ is the imaginary unit. The force per adsorbed particle $\Delta\hat{F} = \Delta\hat{F}_H + m_P\omega U$ is the sum of the hydrodynamic force, $\Delta\hat{F}_H$, and the inertia, $m_P\omega U$, of one adsorbed particle, where U is the (real-valued) quartz velocity amplitude and $m_P = \rho_F(4\pi/3)a^3$ is the mass of one particle, and it is assumed that the particle mass density equals the fluid mass density, ρ_F. The hydrodynamic force per particle, $\Delta\hat{F}_H$, is the force acting on the combined system of N particles and the substrate minus the force acting on the substrate without the particles, divided by N.

We use dimensional analysis to derive the general form of the governing relation between $\Delta\hat{F}_H$ and the operating conditions. The number of variables in the problem is seven, that is, $\Delta\hat{F}_H$, U, ω, a, ϕ, ρ_F, and the fluid kinematic viscosity, ν_F. According to the Buckingham-Pi theorem,[28] one can combine seven variables (with three units being length, time, and mass) into $7 - 3 = 4$ independent dimensionless parameters such that $\hat{\Pi}_i = \Delta\hat{F}_H^{\alpha} U^{\beta}\omega^{\gamma}a^{\delta}\phi^{\varepsilon}\nu_F^{\zeta}\rho_F^{\eta}$, where $i = 1, 2, 3,$ or 4 and $\alpha, \beta, \gamma, \delta, \varepsilon, \zeta,$ and η are determined by requiring that $\hat{\Pi}_i$ be dimensionless. This procedure results in the dimensionless force $\hat{\Pi}_1 = \Delta\hat{F}_H/(\rho_F a^3\omega U)$, the dimensionless size $\Pi_2 = a\omega^{1/2}\nu_F^{-1/2}$, the surface coverage $\Pi_3 = \phi$, and the dimensionless velocity $\Pi_4 = Ua/\nu_F$. The parameter Π_4 is known as the Reynolds number, Re, which is estimated to be $\mathrm{Re} = 10^{-2}$ based on $U = 10^{-1}$ m s^{-1},[29] $a = 10^{-7}$ m (see the Materials and Methods Section) and $\nu_F = 10^{-6}$ m^2 s^{-1}. Since Re is small compared to unity, the problem is independent of Re, and the dimensionless force $\hat{\Pi}_1$ is therefore a dimensionless, complex-valued function of only two dimensionless variables: Π_2 and Π_3, that is, $\hat{\Pi}_1 = \hat{\Pi}_1(\Pi_2, \Pi_3)$. Expressing the dimensionless size as $\Pi_2 = a/\delta$, where the penetration depth is given by $\delta = (2\nu_F/\omega)^{1/2}$, the governing relation is written as

$$\Delta\hat{F}_H = \rho_F a^3\omega U\hat{\Pi}_1\left(\frac{\delta}{a}, \phi\right) \tag{2}$$

As described below, $\hat{\Pi}_1(\delta/a,\phi)$ is determined by using numerical simulation.

MATERIALS AND METHODS

Numerical Simulation. A lattice Boltzmann (LB) method was employed to compute the hydrodynamics of a single spherical particle, with radius a, which is attached to an oscillating surface. The specific details of the LB method are provided in the Supporting Information. The geometry and coordinate system of the simulation setup are presented in Figure 1a. The quartz surface has its normal in the z direction and oscillates in the x direction. The y direction is normal to the x and z directions. The domain sizes are L in the horizontal (x and y) directions and L_z in the vertical (z) direction. In the horizontal directions, periodic boundary conditions are employed. This means that the system represents a periodic array of spheres, with an interparticle separation distance of L. Thus, by varying the horizontal domain size L, we can modulate the particle surface coverage, $\phi = \pi(a/L)^2$.

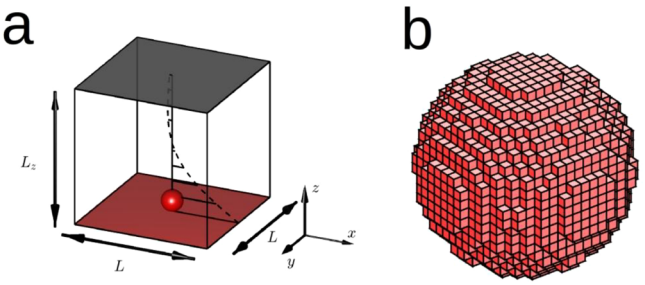

Figure 1. (a) Computational domain of the lattice Boltzmann (LB) simulation. (b) Staircase approximation of a spherical particle in the LB simulation, where the particle radius spans ten lattice spacings.

The numerical method to solve the hydrodynamics problem is based on a three-dimensional staircase approximation of the spherical particle shape, as shown in Figure 1b. The fluid kinematic viscosity was fixed at $\nu_F = \Delta x^2/(6\Delta t)$, where Δx and Δt are the lattice spacing and computational time step, respectively. The simulations were conducted using a range of values for the horizontal and vertical domain sizes, L and L_z, particle radius a, and oscillation frequency f, which resulted in a surface coverage between $\phi \approx 0.01$ and 0.8 and a scaled, viscous penetration depth that varied between $\delta/a \approx 0.6$ and 4.6. All simulation parameters are listed in Supporting Information, Table S1.

DOI: 10.1021/acs.analchem.7b04607
Anal. Chem. 2018, 90, 2238−2245

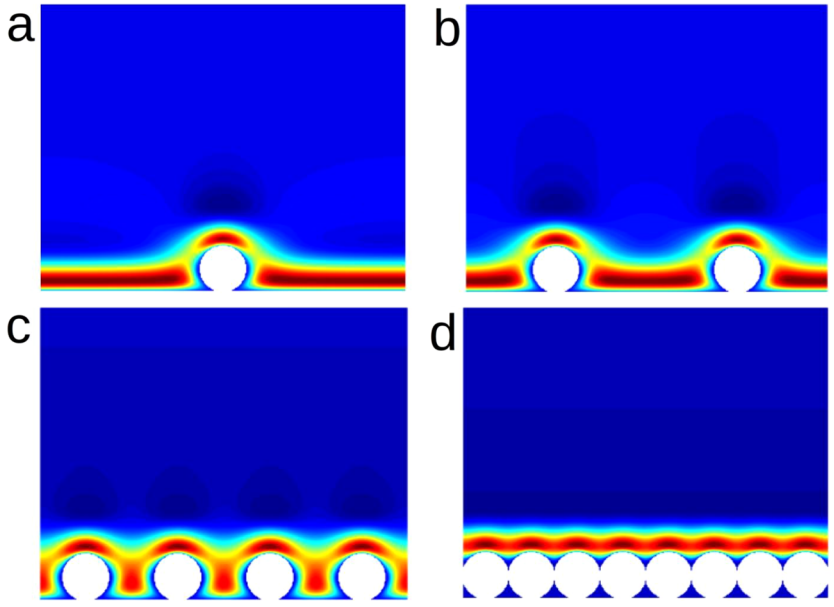

Figure 2. Simulated x-component of the fluid velocity field around spherical particles attached to an oscillating surface at different surface coverages: $\phi \approx$ (a) 0.01, (b) 0.05, (c) 0.2, and (d) 0.8. The snapshots are taken at the instant in the oscillation, when the velocity at the surface equals zero. For all cases, the viscous penetration depth scaled with the particle radius is $\delta/a \approx 0.6$.

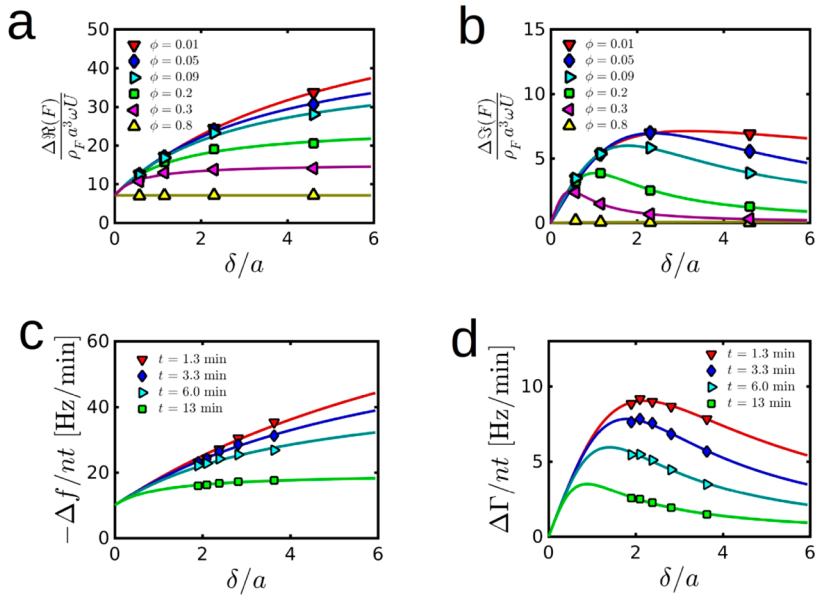

Figure 3. (a) Simulated real part of the QCM force $\Delta\mathcal{R}(\hat{F})$ (corresponding to frequency shift) per particle versus scaled viscous, penetration depth δ/a for various surface coverages ϕ. (b) Simulated imaginary part of QCM force $\Delta\mathcal{J}(\hat{F})$ (corresponding to dissipation shift) per particle vs scaled penetration depth δ/a for various surface coverages ϕ. The simulated force $\Delta\hat{F}$ is scaled with $a^3\rho_F\omega U$, where a is the particle radius, ρ_F is the fluid mass density, ω is the QCM (overtone) angular frequency, and U is the QCM (overtone) velocity amplitude. (c) Measured, negative QCM frequency shift per overtone $-\Delta f/n$ vs scaled penetration depth δ/a for various time points t. (d) Measured QCM bandwidth shift per overtone $\Delta\Gamma/n$ per particle vs scaled penetration depth δ/a for various time points t. In order to compare the experimental data in (c, d) to the simulation data in (a, b), we divided $-\Delta f/n$ and $\Delta\Gamma/n$ by the adsorption time t, which is, prior to saturation, assumed to be proportional to the number of adsorbed particles.

Liposome Preparation. Liposomes (lipid vesicles), which are in the gel phase at room temperature, were prepared by the extrusion method.[30] A dried film of 1,2-dipalmitoyl-*sn*-glycero-3-phosphocholine (DPPC, Avanti Polar Lipids, Alabaster, AL, U.S.A.) lipids was hydrated in an aqueous buffer solution (10 mM Tris [pH 7.5] with 150 mM NaCl) at a lipid concentration of 5 mg/mL, using Milli-Q-treated water with a minimum resistivity of 18.2 MΩ·cm (Millipore, Billerica, MA, U.S.A.). After vortexing the sample, the liposomes were extruded through a track-etched polycarbonate membrane with a 50 nm diameter nominal pore size. As the fluid-to-gel phase transition temperature of the DPPC lipid is around 41 °C, the liposome suspension was heated to ∼60 °C during the extrusion process, so that there was efficient sizing of the DPPC liposomes in the fluid-phase state.[31] After the extrusion process was completed, the DPPC liposome suspension was cooled down to room

DOI: 10.1021/acs.analchem.7b04607
Anal. Chem. 2018, 90, 2238−2245

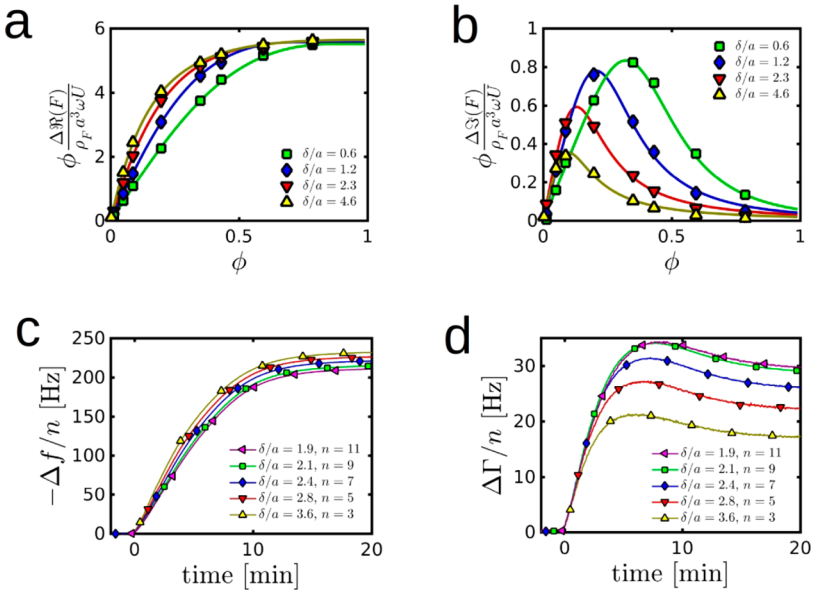

Figure 4. (a) Simulated real part of QCM force per πa^2 surface area $\phi\Delta\mathcal{R}(\hat{F})$ (corresponding to frequency shift), as a function of surface coverage ϕ, for various scaled penetration depths δ/a. (b) Simulated imaginary part of QCM force per πa^2 surface area $\phi\Delta\mathcal{J}(\hat{F})$ (corresponding to dissipation shift), as a function of surface coverage ϕ, for various scaled penetration depths δ/a. (c) Measured QCM frequency shift per overtone $-\Delta f/n$ as a function of time for various overtones n, corresponding to various scaled penetration depths δ/a. (d) Measured QCM bandwidth shift per overtone $\Delta\Gamma/n$ as a function of time for various overtones n, corresponding to various scaled penetration depths δ/a.

temperature, and the liposomes returned to the gel-phase state. The size of the liposome radius, a, was measured by dynamic light scattering (DLS, Brookhaven Instruments, Holtsville, NY, U.S.A.), and the mean and standard deviation were determined to be a = 38 ± 7 nm. The corresponding size distribution is given in Supporting Information, Figure S1. Immediately before QCM experiments, the liposomes were diluted to a 0.05 mg/mL lipid concentration in 10 mM Tris buffer [pH 7.5] with 250 mM NaCl. The selected ionic strength promotes a strong adhesion force by shielding electrostatic repulsion between the TiO_2-coated substrate and DPPC liposomes,[32] while it should also be noted that the adsorbed, gel-phase DPPC liposomes remain spherical and do not deform appreciably under these conditions.[33]

QCM Experiments. Liposome adsorption was measured by using the Q-Sense E4 QCM instrument (Biolin Scientific AB, Stockholm, Sweden). We used quartz crystal sensor chips, which had a sputter-coated, 50 nm thick layer of TiO_2 (model No. QSX 310, Biolin Scientific AB) and a fundamental frequency of f_0 = 5 MHz, thickness of l_Q = 0.3 mm, and mass density of ρ_Q = 2.65 g/mL. A peristaltic pump (Reglo Digital, Ismatec, Glattbrugg, Switzerland) was used to inject liquid sample into the measurement chamber at a flow rate of 50 μL/min. The temperature in the measurement chamber was maintained at 25.0 ± 0.5 °C. The experimental data were collected at the third to 11th odd overtones using the QSoft software program (Biolin Scientific AB). Baseline signals in aqueous buffer solution (without liposomes) were recorded for 7 min prior to liposome injection under continuous flow conditions.

RESULTS

Flow Field Visualizations. Figure 2 shows the simulated x-component of the fluid velocity in the (x, z)-plane for four different values of ϕ at a fixed value of $\delta/a \approx 0.6$. These visualizations illustrate the physical mechanism that is responsible for the overtone- and time-dependent frequency and bandwidth shifts, which are typically observed during particle adsorption. Below, we analyze these dependencies in detail, through both simulation and experiment.

QCM Response as a Function of Overtone Number. In Figure 3a,b, we investigate the simulated QCM force per particle, $\Delta\hat{F}$, as a function of the scaled penetration depth, δ/a, for various fixed values of ϕ. As mentioned above, $\Delta\hat{F}$ is a complex-valued force amplitude, and the real and imaginary parts correspond to the QCM frequency and bandwidth shifts, respectively (cf. eq 1). Figure 3a shows the real part $\Delta\mathcal{R}(\hat{F})$, which is the sum of the inertial force of the particle and that of the coupled fluid. The results indicate that, for large $\phi \approx 0.8$, $\Delta\mathcal{R}(\hat{F})$ is independent of the penetration depth. In this regime, $\Delta\mathcal{R}(\hat{F})$ consists solely of particle inertia, while there is no contribution from the coupled fluid, that is, the coupled fluid resembles that of a flat surface, which can be seen from the visualization as presented in Figure 2d. On the other hand, at low $\phi \approx 0.01$, $\Delta\mathcal{R}(\hat{F})$ contains the particle inertia (constant component as a function of δ/a) as well as the inertia of the coupled fluid, which is reflected by an increase of $\Delta\mathcal{R}(\hat{F})$ as a function of δ/a. However, it is observed that $\Delta\mathcal{R}(\hat{F})$ does not continually increase as δ/a becomes larger. At large δ/a, $\Delta\mathcal{R}(\hat{F})$ levels off, which reflects the hydrodynamic interactions between neighboring particles, that is, the overlap of the coupled fluid of neighboring particles. With increasing ϕ, the distance between neighboring particles decreases, and the hydrodynamic coupling is therefore observed to set in at smaller δ/a.

Figure 3b shows the imaginary part of the force per particle, $\Delta\mathcal{J}(\hat{F})$, which measures the frictional force of the coupled fluid that is exerted at the solid−fluid interface. For $\phi \approx 0.8$, the particles form a densely packed layer (cf. Figure 2d) and the friction resembles that occurring on a flat surface, that is, $\Delta\mathcal{J}(\hat{F}) = 0$. On the other hand, for smaller ϕ, $\Delta\mathcal{J}(\hat{F})$ first

DOI: 10.1021/acs.analchem.7b04607
Anal. Chem. 2018, 90, 2238−2245

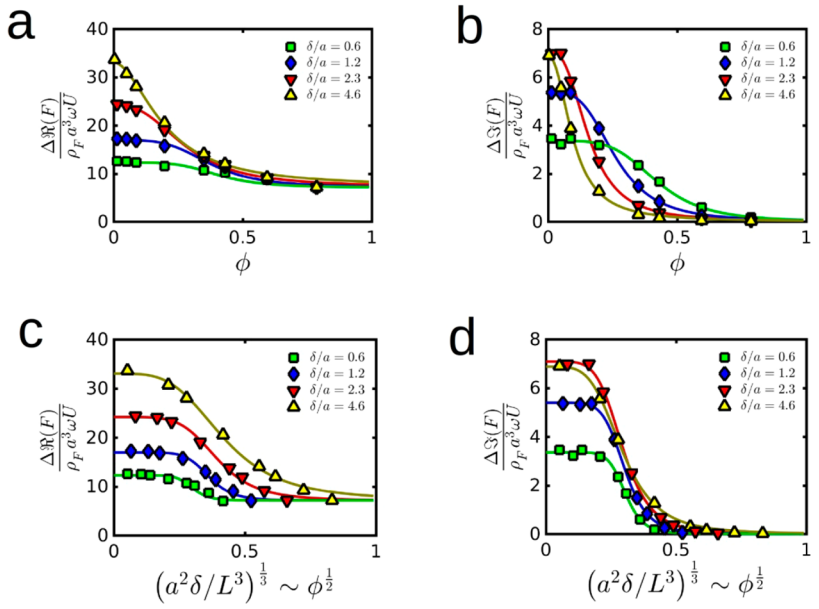

Figure 5. (a) Simulated real part of the QCM force per particle $\Delta\mathcal{R}(\hat{F})$ as a function of the surface coverage ϕ for various values of the scaled penetration depth δ/a. (b) Simulated imaginary part of the QCM force per particle $\Delta\mathcal{J}(\hat{F})$ as a function of the surface coverage ϕ for various values of the scaled penetration depth δ/a. (c) Simulated real part of the QCM force per particle $\Delta\mathcal{R}(\hat{F})$ as a function of the scaled interaction length $(a^2\delta)^{1/3}/L$ for various values of the scaled penetration depth δ/a. (d) Simulated imaginary part of the QCM force per particle $\Delta\mathcal{J}(\hat{F})$ as a function of the scaled interaction length $(a^2\delta)^{1/3}/L$ for various values of the scaled penetration depth δ/a.

increases and then decreases toward zero due to the overlap of the coupled fluid of the neighboring particles.

Figure 3c,d shows the experimentally measured force per particle as a function of δ/a, which corresponds to various overtones n, and for various ϕ, which corresponds to various time points t. The relative penetration depth, δ/a, is related to the overtone, n, by $\delta/a = (\nu_F/\pi f_0 n a^2)^{1/2}$. The real and imaginary parts of the force are represented by the (negative) frequency shift per overtone number, $-\Delta f/n$, and by the bandwidth shift per overtone number, $\Delta\Gamma/n$. These quantities correspond to the force induced by all adsorbed particles. In order to obtain quantities that are proportional to the force per adsorbed particle, we need to divide $-\Delta f/n$ and $\Delta\Gamma/n$ by the (areal) number (density) of adsorbed particles. Since the number density of adsorbed liposomes is not directly available, we take into account that the liposome adsorption process is diffusion-limited,[34] which implies that the number density is proportional to the adsorption time t. For this reason, we divide the frequency and bandwidth shifts (per overtone number) in Figure 3c,d by t. Under diffusion-limited adsorption conditions, the resulting quantities, $-\Delta f/nt$ and $\Delta\Gamma/nt$, are equal to the force per particle, up to an unknown proportionality constant. We do not further consider this constant, but focus on qualitatively comparing the simulated and measured QCM force dependencies on δ/a and ϕ. The experimental data in Figure 3c,d compare well with the simulated data in Figure 3a,b in terms of the aforementioned dependencies on δ/a and ϕ.

QCM Response as a Function of Time. We now turn our attention to the time dependence of the frequency and bandwidth shifts due to the entire ensemble of adsorbed particles. For this purpose, we multiply the real, $\mathcal{R}$, and imaginary, $\mathcal{J}$, parts of the simulated force per particle (cf. Figure 3a,b) by the surface coverage, ϕ. In Figure 4a,b, we plot the resulting $\phi\Delta\mathcal{R}(\hat{F})$ and $\phi\Delta\mathcal{J}(\hat{F})$ as functions of ϕ, for various δ/a. Experimentally, this representation corresponds (up to an unknown proportionality constant) to the frequency and bandwidth shifts as functions of time for the various overtones, which are shown for comparison in Figure 4c,d.

The simulated inertial force on the QCM response increases monotonically with ϕ and with δ/a (Figure 4a), and these trends agree well with the experimental data (Figure 4c). At saturation coverage, the different overtones collapse, that is, the saturated layer of regularly distributed particles behaves as a uniform film.[9] In the experiment, one nuance is that the different overtones do not collapse at saturation, which reflects that the saturated layer of adsorbed liposomes does not fully behave as a uniform film. This difference might reflect the irregular, spatial particle arrangement, with gaps between the particles, as opposed to the regular and closely packed particle arrangement in the simulation.

The simulated frictional force on the QCM response is a nonmonotonic function of ϕ, which increases at low ϕ and decreases toward zero at high ϕ (Figure 4b). These trends are also observed in the experimental data, albeit the decrease at higher ϕ does not continue to zero but instead saturates at a finite value (Figure 4d). This again indicates that the saturated layer is not closely packed.

It is noted that the transient maximum in the bandwidth shift (cf. Figure 4b,d) has been observed previously for globular proteins and virus particles, in which case it was attributed to the softness of the linkers between the particles and the substrate.[3,27] Interestingly, the present results support that similar transient maxima occur in purely rigid systems, originating from the hydrodynamic interactions between particles and, hence, provide a physical mechanism to explain past experimental observations with adsorbed liposomes as well.[24,33]

Onset of Hydrodynamic Coupling. We continue by studying the relation between the hydrodynamic force per particle and the average distance between the particles, L =

DOI: 10.1021/acs.analchem.7b04607
Anal. Chem. 2018, 90, 2238−2245

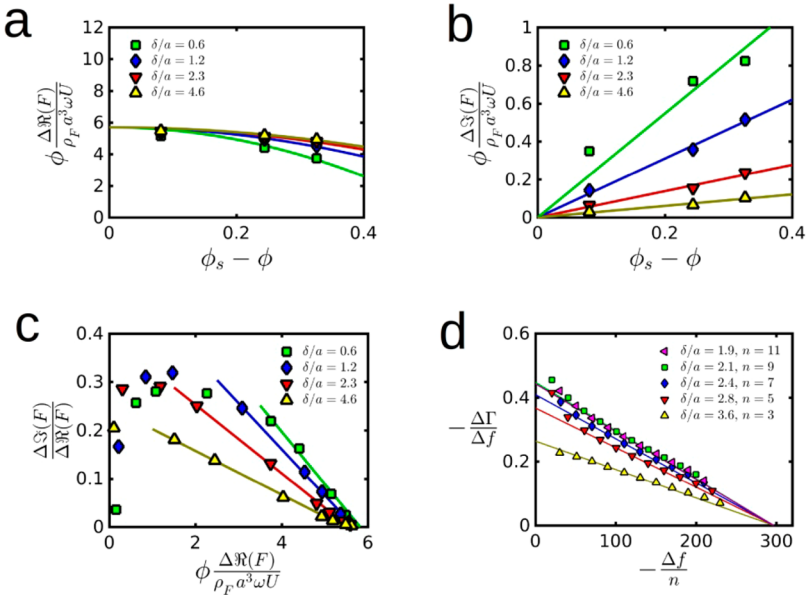

Figure 6. (a) Simulated real part of QCM force per πa^2 surface area $\phi\Delta\mathcal{R}(\hat{F})$ (corresponding to frequency shift), as a function of the void fraction $\phi' = \phi_S - \phi$, for various scaled penetration depths δ/a. (b) Simulated imaginary part of QCM force per πa^2 surface area $\phi\Delta\mathcal{J}(\hat{F})$ (corresponding to dissipation shift), as a function of the void fraction $\phi' = \phi_S - \phi$, for various scaled penetration depths δ/a. The data are fitted by linear functions that intercept the origin when choosing $\phi_S \approx 0.7$. (c) Simulated ratio of imaginary and real parts of the QCM force as a function of the real part of the force density. In agreement with eq 7, the data for different δ/a follow linear trends that intercept the horizontal at the same point. (d) Experimental ratio of bandwidth shift $\Delta\Gamma$ and negative frequency shift $-\Delta f$ as a function of negative frequency shift per overtone $-\Delta f/n$ for various overtones (corresponding to various δ/a). The data for the different overtones follow linear trajectories, which intercept the horizontal axis at a frequency shift that, according to eqs 8 and 9, corresponds to a saturation surface coverage of $\phi_S \approx 0.6$.

$a(\pi/\phi)^{1/2}$, or equivalently, the surface coverage ϕ. To this end, for various fixed values of δ/a, the simulated inertial force $\Delta\mathcal{R}(\hat{F})$ and frictional force $\Delta\mathcal{J}(\hat{F})$ per particle are presented as functions of ϕ in Figure 5a and b, respectively. For small ϕ (or large L), there is no hydrodynamic coupling between the particles, and hence, the forces are independent of ϕ. With increasing ϕ, the separation between adsorbed particles decreases and hydrodynamic coupling sets in above a critical ϕ^*, as reflected by decreases in $\Delta\mathcal{R}(\hat{F})$ and $\Delta\mathcal{J}(\hat{F})$ as functions of ϕ. Since the volume of the coupled fluid per particle increases with increasing δ (cf. Figure 3a), the critical ϕ^*, which marks the onset of hydrodynamic coupling, decreases with increasing δ/a (cf. Figure 5a,b). As the volume of the coupled fluid scales as $a^2\delta$ (cf. Figure 3a), we define the interaction length scale as $l \sim (a^2\delta)^{1/3}$, and equating this length scale with the interparticle distance, $L \sim a\phi^{-1/2}$, provides an onset condition for hydrodynamic coupling, $\phi^* \sim (a/\delta)^{2/3}$. To test this scaling hypothesis, plots of $\Delta\mathcal{R}(\hat{F})$ and $\Delta\mathcal{J}(\hat{F})$ are presented in Figure 5c and d, respectively, as functions of $l/L \sim (a^2\delta/L^3)^{1/3}$ for various δ/a. Hydrodynamic coupling is evident from the decreases in $\Delta\mathcal{R}(\hat{F})$ and $\Delta\mathcal{J}(\hat{F})$ that occur beyond $(a^2\delta/L^3)^{1/3} \approx 0.25$, and this value is independent of δ/a, which validates the proposed interaction length scale, $l \sim (a^2\delta)^{1/3}$.

Theoretical Basis for the $\Delta\Gamma/\Delta f$ Extrapolation Method. It is noted that the present simulation is based on the assumption of a regular spatial distribution of particles, and the corresponding hydrodynamic interactions are weaker than in the more realistic case of a random distribution, see, for example, refs 16 and 20. However, the qualitative behavior of the hydrodynamic interaction does not depend on the details of the spatial distribution, as demonstrated by the agreement between simulation and experiment in Figures 3 and 4.

This agreement supports the significance of the simulations for QCM data analysis. Consequently, we now analyze the asymptotic behavior of the simulations when ϕ approaches the saturation density, ϕ_S, and provide a theoretical basis for the $\Delta\Gamma/\Delta f$ extrapolation method to extract particle sizes from QCM data at high surface coverage.[23] We start by recalling that the frequency and bandwidth shifts are proportional to the real and imaginary components, respectively, of the force density, $\phi\Delta\hat{F}$, which is the force per πa^2 surface area of the QCM response. Using $N = A_Q\phi/\pi a^2$, eq 1 can be rewritten as

$$-\Delta f + i\Delta\Gamma = \frac{f\phi\Delta\hat{F}}{\pi a^2 l_Q \varrho_Q U\omega} \tag{3}$$

In Figure 6a, it seen that for $\phi \to \phi_S$, the real part $\phi\Delta\mathcal{R}(\hat{F})$ approaches a constant that is independent of δ/a, that is, $\phi\Delta\mathcal{R}(\hat{F}) \to \chi_R\phi\rho_F\omega U a^3$. This situation resembles the rigid oscillation of a homogeneous film (cf. Figure 2d). Figure 6b shows that the imaginary part of the force density $\phi\Delta\mathcal{J}(\hat{F}) \to 0$, when $\phi \to \phi_S$. If we choose $\phi_S \approx 0.7$, then the relation between $\phi\Delta\mathcal{J}(\hat{F})$ and the void fraction $\phi' = \phi_S - \phi$ is linear for small ϕ', that is, $\phi\Delta\mathcal{J}(\hat{F}) \to \chi_I\rho_F\omega U a^3\phi'$, which is shown by the straight lines in Figure 6b. Here the proportionality constant χ_I is seen to depend on δ/a. It is noted that the saturation surface coverage, ϕ_S, beyond which the adlayer behaves as a uniform and rigid film, is slightly smaller than the value at close packing of the current system, $\phi_S \approx 0.8$. Furthermore, it is expected that the value for ϕ_S varies under different experimental conditions, including the size distribution and spatial distribution of adsorbed particles. Inserting the above-mentioned scaling relations for the real and imaginary parts of $\Delta\hat{F}$ into eq 3, we find

DOI: 10.1021/acs.analchem.7b04607
Anal. Chem. 2018, 90, 2238−2245

$$-\frac{\Delta f}{n} \approx \chi_R \frac{f_0 \rho_F a}{\pi \rho_Q l_Q}(\phi_S - \phi') \tag{4}$$

and

$$\frac{\Delta \Gamma}{n} \approx \chi_I \frac{f_0 \rho_F a}{\pi \rho_Q l_Q}\phi' \tag{5}$$

Dividing eq 5 by eq 4 and Taylor expanding the result up to the first order in ϕ':

$$-\frac{\Delta \Gamma}{\Delta f} \approx \frac{\chi_I \phi'}{\chi_R \phi_S} \tag{6}$$

and combining eqs 4 and 6 yields

$$-\frac{\Delta \Gamma}{\Delta f} \approx \frac{\chi_I}{\chi_R}\left(1 + \frac{\Delta f \pi \rho_Q l_Q}{n f_0 \chi_R \phi_S \rho_F a}\right) \tag{7}$$

that is, on $(-\Delta f/n, -\Delta\Gamma/\Delta f)$ coordinates, the QCM data appear as a straight line that intercepts the horizontal at

$$-\frac{\Delta f}{n} = \frac{f_0 \rho_F h}{\rho_Q l_Q} \tag{8}$$

and corresponds to the frequency shift for a uniform layer with a thickness of

$$h = \frac{a \chi_R \phi_S}{\pi} \tag{9}$$

Importantly, this result provides a theoretical basis for the $-\Delta\Gamma/\Delta f$ extrapolation method in order to determine the particle size from QCM data at high surface coverages.[23,24]

Figure 6c shows numerical data on $\left[\frac{\phi \Delta \mathcal{R}(\hat{F})}{\rho_F a^3 \omega U}, \frac{\Delta \mathcal{J}(\hat{F})}{\Delta \mathcal{R}(\hat{F})}\right]$ coordinates, which are equivalent (up to some proportionality constants) to the $(-\Delta f/n, -\Delta\Gamma/\Delta f)$ coordinates. On these equivalent coordinates, the numerical data for the different overtones (different δ/a values) are observed to follow linear trajectories, which intercept the horizontal at the same point, in agreement with eq 7. Interestingly, while the linear relation (eq 7) was derived by assuming $\phi' \ll 1$, the numerical data in Figure 6c follow a linear relationship for nearly the entire domain, especially for relatively large $\delta/a \geq 2$. The same is observed in the experimental data in Figure 6d, where according to eq 7, the intercept at $-\Delta f/n \approx 300$ Hz corresponds to a saturation density of $\phi_S \approx 0.6$ using $a = 38$ nm and $\chi_R = 7.1$.

Effect of Particle Polydispersity. Let us finally comment on the effect of particle polydispersity. Olsson et al. used the $\Delta\Gamma/\Delta f$ extrapolation method to measure the effective film height (h in eq 8) of a bimodal mixture of spheres, with radii of $a_1 = 13$ nm and $a_2 = 55$ nm, respectively, using various sphere number ratios N_1/N_2.[25] Their measured, effective particle radius $a_{eff} = h/2$ was well captured by

$$a_{eff} = \frac{N_1 a_1^3 + N_2 a_2^3}{N_1 a_1^2 + N_2 a_2^2} \tag{10}$$

which corresponds to the frequency shift that one would obtain in vacuum, that is, proportional to particle volume (numerator) per area (denominator). We generalize eq 10 to the case of a continuous particle size distribution $N(a)$:

$$a_{eff} = \frac{\int N(a) a^3 \mathrm{d}a}{\int N(a) a^2 \mathrm{d}a} \tag{11}$$

and estimate the effect of polydispersity on the effective particle radius, as obtained by the $\Delta\Gamma/\Delta f$ extrapolation method, applied to our QCM data. In the present case, the particle radius has a mean value of $\bar{a} = 38$ nm and standard deviation of $a' = 7$ nm. The particle size distribution (measured by DLS) is log-normal (cf. Figure S1). However, when $(a'/a)^2 \ll 1$, the log-normal can be approximated by the Gaussian:

$$N(a) \sim \exp\left[-\frac{(a - \bar{a})^2}{2a'^2}\right] \tag{12}$$

Since $(a'/\bar{a})^2 \approx 0.03 \ll 1$, eqs 11 and 12 give an effective particle radius of $a_{eff} \approx \bar{a}[1 + 2(a'/\bar{a})^2]$, which is estimated to be 7% larger than the mean value $\bar{a}$.

It is finally noted that the particle flux J from the bulk solution to the QCM-D surface is limited by diffusion,[34] and according to boundary layer theory:[35] $J \sim a^{-2/3}$. Therefore, the size distribution on the surface $N_s(a)$ differs from that in the bulk $N(a)$:

$$N_s(a) \sim N(a) a^{-2/3} \tag{13}$$

Combining eqs 12 and 13 and dropping the (irrelevant) constant terms in the exponent give

$$N_s(a) \sim \exp\left[-\frac{\left(a - \bar{a}\left[1 - \frac{2}{3}\left(\frac{a'}{\bar{a}}\right)^2\right]\right)^2}{2a'^2}\right] \tag{14}$$

This means that the surface size distribution has a mean value of $\bar{a}_s \approx \bar{a}\left(1 - \frac{2}{3}(a'/\bar{a})^2\right)$, which is 2% smaller than in the bulk. Since this effect is small and counteracting the first (~7%) effect, we conclude that, in the present QCM experiments, polydispersity has a minor effect on the effective particle height obtained from the $\Delta\Gamma/\Delta f$ extrapolation method.

CONCLUSION

We have conducted numerical simulations of the hydrodynamics of spherical particles that are attached to an oscillating surface across a range of surface coverage values, ϕ, and scaled penetration depths, δ/a. The simulations compare well to experimental QCM data of adsorbed gel-phase liposomes (38 nm mean radius), offering a quantitative framework to understand how hydrodynamic coupling between adsorbed particles influences QCM measurement responses. In particular, the numerical data show that hydrodynamic coupling between particles sets in beyond a critical surface coverage, $\phi^* \sim (a/\delta)^{2/3}$. The effect of the coupling is a decrease in the contribution per particle to both the frequency and the bandwidth shifts. Guided by the simulation outcome, and by expanding the frequency and bandwidth shifts in the void fraction (space between particles), we derived a theoretical basis for the $\Delta\Gamma/\Delta f$ extrapolation method, further validating its utility for extracting particle size from QCM data collected at high surface coverages.

DOI: 10.1021/acs.analchem.7b04607
Anal. Chem. 2018, 90, 2238−2245

■ ASSOCIATED CONTENT

Supporting Information

The Supporting Information is available free of charge on the ACS Publications website at DOI: 10.1021/acs.analchem.7b04607.

Additional details about the lattice Boltzmann simulations, including simulation parameters (PDF).

■ AUTHOR INFORMATION

Corresponding Author

*E-mail: njcho@ntu.edu.sg.

ORCID

Nam-Joon Cho: 0000-0002-8692-8955

Notes

The authors declare no competing financial interest.

■ ACKNOWLEDGMENTS

This work was supported by the National Research Foundation (NRF2015NRF-POC001-019).

■ REFERENCES

(1) Martin, S. J.; Granstaff, V. E.; Frye, G. C. *Anal. Chem.* **1991**, *63*, 2272−2281.
(2) Marx, K. A. *Biomacromolecules* **2003**, *4*, 1099−1120.
(3) Reviakine, I.; Johannsmann, D.; Richter, R. P. *Anal. Chem.* **2011**, *83*, 8838−8848.
(4) Johannsmann, D. *The Quartz Crystal Microbalance in Soft Matter Research: Fundamentals and Modeling*; Springer, 2014.
(5) Rodahl, M.; Höök, F.; Krozer, A.; Brzezinski, P.; Kasemo, B. *Rev. Sci. Instrum.* **1995**, *66*, 3924−3930.
(6) Rodahl, M.; Kasemo, B. *Rev. Sci. Instrum.* **1996**, *67*, 3238−3241.
(7) Keller, C.; Kasemo, B. *Biophys. J.* **1998**, *75*, 1397−1402.
(8) Cho, N.-J.; Frank, C. W.; Kasemo, B.; Höök, F. *Nat. Protoc.* **2010**, *5*, 1096−1106.
(9) Sauerbrey, G. *Eur. Phys. J. A* **1959**, *155*, 206−222.
(10) Voinova, M. V.; Rodahl, M.; Jonson, M.; Kasemo, B. *Phys. Scr.* **1999**, *59*, 391.
(11) Johannsmann, D. *Macromol. Chem. Phys.* **1999**, *200*, 501−516.
(12) Reviakine, I.; Rossetti, F. F.; Morozov, A. N.; Textor, M. *J. Chem. Phys.* **2005**, *122*, 204711.
(13) Urbakh, M.; Tsionsky, V.; Gileadi, E.; Daikhin, L. *Piezoelectric Sensors*; Springer, 2006; pp 111−149.
(14) Fang, J.; Ren, C.; Zhu, T.; Wang, K.; Jiang, Z.; Ma, Y. *Analyst* **2015**, *140*, 1323−1336.
(15) Rojas, E.; Gallego, M.; Reviakine, I. *Anal. Chem.* **2008**, *80*, 8982−8990.
(16) Bingen, P.; Wang, G.; Steinmetz, N. F.; Rodahl, M.; Richter, R. P. *Anal. Chem.* **2008**, *80*, 8880−8890.
(17) Johannsmann, D.; Reviakine, I.; Rojas, E.; Gallego, M. *Anal. Chem.* **2008**, *80*, 8891−8899.
(18) Carton, I.; Brisson, A. R.; Richter, R. P. *Anal. Chem.* **2010**, *82*, 9275−9281.
(19) Grunewald, C.; Schmudde, M.; Noufele, C. N.; Graf, C.; Risse, T. *Anal. Chem.* **2015**, *87*, 10642−10649.
(20) Johannsmann, D.; Brenner, G. *Anal. Chem.* **2015**, *87*, 7476−7484.
(21) Gillissen, J. J. J.; Tabaei, S. R.; Jackman, J. A.; Cho, N.-J. *Analyst* **2017**, *142*, 3370−3379.
(22) Gillissen, J. J. J.; Jackman, J. A.; Tabaei, S. R.; Yoon, B. K.; Cho, N.-J. *Anal. Chem.* **2017**, na.
(23) Tellechea, E.; Johannsmann, D.; Steinmetz, N. F.; Richter, R. P.; Reviakine, I. *Langmuir* **2009**, *25*, 5177−5184.
(24) Reviakine, I.; Gallego, M.; Johannsmann, D.; Tellechea, E. *J. Chem. Phys.* **2012**, *136*, 084702.
(25) Olsson, A. L.; Quevedo, I. R.; He, D.; Basnet, M.; Tufenkji, N. *ACS Nano* **2013**, *7*, 7833−7843.
(26) Zhu, T.; Jiang, Z.; Nurlybaeva, E. M. R.; Sheng, J.; Ma, Y. *Langmuir* **2013**, *29*, 6377−6385.
(27) Johannsmann, D.; Reviakine, I.; Richter, R. P. *Anal. Chem.* **2009**, *81*, 8167−8176.
(28) Barenblatt, G. I. *Scaling, Self-Similarity, and Intermediate Asymptotics: Dimensional Analysis and Intermediate Asymptotics*; Cambridge University Press, 1996.
(29) Arnau, A. *Piezoelectric Transducers and Applications*; Springer, 2004.
(30) MacDonald, R. C.; MacDonald, R. I.; Menco, B. P. M.; Takeshita, K.; Subbarao, N. K.; Hu, L.-R. *Biochim. Biophys. Acta, Biomembr.* **1991**, *1061*, 297−303.
(31) Nayar, R.; Hope, M. J.; Cullis, P. R. *Biochim. Biophys. Acta, Biomembr.* **1989**, *986*, 200−206.
(32) Jackman, J. A.; Zan, G. H.; Zhao, Z.; Cho, N.-J. *Langmuir* **2014**, *30*, 5368−5372.
(33) Jackman, J. A.; Yorulmaz Avsar, S.; Ferhan, A. R.; Li, D.; Park, J. H.; Zhdanov, V. P.; Cho, N.-J. *Anal. Chem.* **2017**, *89*, 1102−1109.
(34) Keller, C.; Glasmästar, K.; Zhdanov, V.; Kasemo, B. *Phys. Rev. Lett.* **2000**, *84*, 5443−5446.
(35) Schlichting, H. *Boundary-Layer Theory*; McGraw-Hill, 1968.

DOI: 10.1021/acs.analchem.7b04607
Anal. Chem. 2018, 90, 2238−2245